CFD Simulations of the Pazy Wing in Support of the Third Aeroelastic Prediction Workshop

Fehrs, Michael; Ritter, Markus; Helm, Sebastian; Mertens, C.

Publication date
2022

Document Version
Final published version

Published in
International Forum on Aeroelasticity and Structural Dynamics

Citation (APA)
Fehrs, M., Ritter, M., Helm, S., & Mertens, C. (2022). CFD Simulations of the Pazy Wing in Support of the Third Aeroelastic Prediction Workshop. In *International Forum on Aeroelasticity and Structural Dynamics* Article IFASD-2022-156

International Forum on Aeroelasticity and Structural Dynamics
IFASD 2022
13-17 June 2022, Madrid, Spain

CFD SIMULATIONS OF THE PAZY WING IN SUPPORT OF THE THIRD AEROELASTIC PREDICTION WORKSHOP

Michael Fehrs[1], Markus Ritter[1], Sebastian Helm[1], Christoph Mertens[2]

[1]German Aerospace Center (DLR), Institute of Aeroelasticity, Göttingen, Germany
michael.fehrs@dlr.de, markus.ritter@dlr.de, sebastian.helm@dlr.de

[2]Faculty of Aerospace Engineering, Delft University of Technology, 2629 HS Delft, The Netherlands
c.mertens@tudelft.nl

Keywords: CFD, Free Transition, Gamma Transition Model, SST Turbulence Model, Low Reynolds, Pazy Wing, Aeroelastic Prediction Workshop

Abstract: The *Pazy Wing* test case is a benchmark for the investigation of aeroelastic effects at very large deflections. Tip deformations in the order of 50% span were measured in wind tunnel tests, which renders this model highly attractive for the validation of numerical aeroelastic methods and tools for geometrically nonlinear, large deflection analyses. Due to the low flow velocity (up to 60 m/s) and the simple geometry of the wing, simulation programs based on subsonic, linear potential aerodynamic solvers (such as VLM and UVLM) are an ideal basis for static coupling and flutter simulations. However, more comprehensive analyses with focus on aerodynamic nonlinearities such as stall and limit cycle oscillations (which have been observed in several wind tunnel tests) are attractive research topics but call for advanced aerodynamic methods. The present work is thus focused on high fidelity aerodynamic simulations of the Pazy Wing using RANS with transition modeling in order to capture nonlinear effects originating from the particular shape of the wing and the low Reynolds number. It is a collaborative activity of DLR, NASA, and TU Delft and supports the *Large Deflection Working Group* (LDWG), which is one of the sub-groups of the 3rd *Aeroelastic Prediction Workshop* (AePW3)[1].

1 MOTIVATION AND INTRODUCTION

Detailed information about the Pazy Wing and the LDWG are given in recent publications [1–5]. The Pazy Wing wind tunnel models from Technion and TU Delft (the model investigated in this work) are shown in Fig. 1, the main dimensions are listed in Table 1. Aeroelastic simulations (static coupling and flutter) that have been presented in the LDWG to analyze the behavior of the Pazy Wing are based on geometrically nonlinear structural methods – which are indispensable for this test case – and linear (potential) aerodynamics, mostly the UVLM and the DLM are applied. This combination offers advantages such as low computational cost, and yields surprisingly good agreements with experimental data in terms of steady deflections and stability boundaries. A new field, which is explored by current simulations, is limit cycle oscillations (LCO), which have been observed in several wind tunnel tests. LCOs are an inherently nonlinear phenomenon, and, relating to the Pazy Wing test case, are primarily induced by particular steady and unsteady viscous effects such as laminar separation bubbles, transition mechanisms, and (dynamic) stall. Furthermore, these nonlinearities strongly depend on the local shape of the

[1]https://nescacademy.nasa.gov/workshops/AePW3/public

Table 1: Selected dimensions of the Pazy Wing.

Property	Unit	Pazy Wing
Span	m	0.56
Chord (without tip rod)	m	0.1
Clamping section height	m	0.021
Clamping section diameter	m	0.12
Tip rod length	m	0.3
Tip rod diameter	m	0.01
Airfoil	-	NACA 0018

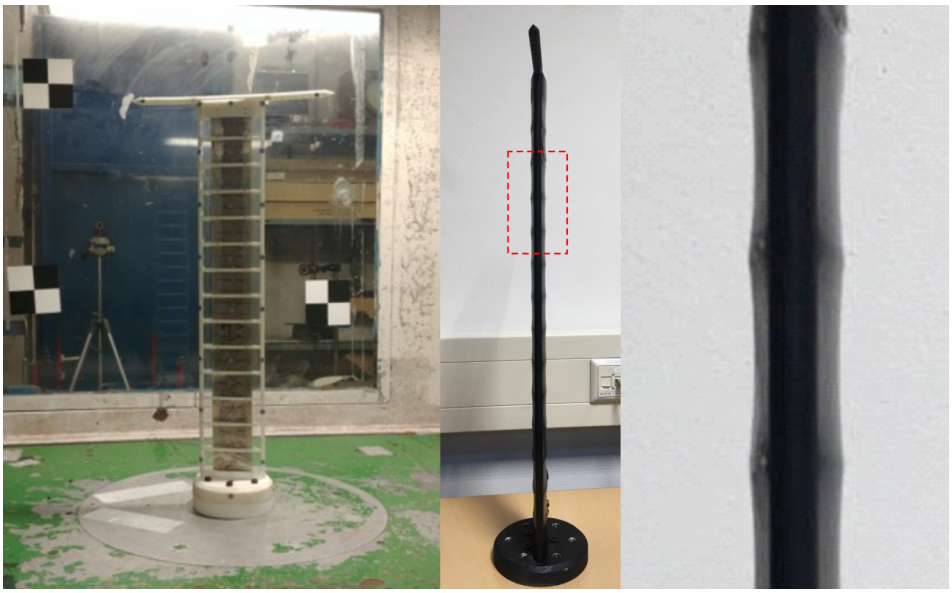

Figure 1: Pazy Wing in wind tunnel at Technion (left) [1]. Outer surface of the Pazy Wing from TU Delft in undeflected jig-shape with close up highlighting the sagging skin (foil cover) between the ribs.

wing's covering (a plastic thermal shrink film) which changes based on the instantaneous flow and structural conditions. Even at the unloaded state, the outer shape of the wing is complex due to the sagging of the foil covering between the ribs which yields a different airfoil section with reduced thickness and kinks. To investigate the aerodynamic effects resulting from these specifics and to address them in future aeroelastic simulations of the Pazy Wing, the potential aerodynamic methods, which have been used by the authors to date, are replaced by CFD-based aerodynamics that solve the RANS and URANS equations with proper methods for the modeling of transition and turbulence.

The objective of this work is to investigate the steady aerodynamic characteristics of the rigid Pazy Wing in jig-shape (no structural deformations are taken into account) based on CFD computations for fully turbulent and transitional boundary layer flows. To account for the true geometry of the wing – including local kinks and the sagging of the foil covering – a scan of the outer geometry of the TU Delft Pazy Wing was used as basis for the CFD grid generation. The insights acquired yield a better understanding of the flow physics of built up (rib) wings with complex outer shapes at low Reynolds numbers.

The DLR TAU-Code [6] is used for the steady RANS computations to analyze the rigid wing in jig-shape. The fully turbulent results are computed with the SST $k-\omega$ turbulence model [7].

Transition prediction is done with the correlation-based γ transition model [8] in combination with the SST k-ω turbulence model. The γ transition model computes the intermittency variable γ in the whole flow field, thus no spanwise locations for the boundary layer stability analyses have to be prescribed as is the case for the e^N method in the TAU transition module [9].

2 WORKFLOW FOR THE CFD GRID GENERATION

To obtain detailed insight into the flow physics of the Pazy Wing, a sophisticated workflow for the generation of the CFD grid was employed. Due to the built-up rib structure and the foil covering of the wing, the shape of the real wind tunnel model deviates significantly from the theoretical (CAD) model – which is designed from a NACA 0018 airfoil section and is used as the basis for manufacturing. For the real wind tunnel model, the 3D printed rib structure is covered by *Oralight*, a plastic film used for radio controlled aircraft applications. The film is applied (glued) onto the structure by heat (iron and heat gun) and shrinks once the heat source is removed. A prestressing is introduced by this approach which ensures a smooth surface even if loads are applied and the structure is deformed slightly. Nevertheless, an unavoidable deviation of the surface is introduced by this process because the foil sags between the ribs which leads to a modified airfoil section whose shape varies depending on the lateral position between the ribs. The outer surface of the Pazy Wing wind tunnel model from TU Delft, depicted in Fig. 2, clearly shows the sagging of the wing's foil covering. The end of the (solid) leading edge in the region between the ribs is marked by a kink (which is detailed in Fig. 2). Such details influence the flow locally and, as will be shown in the following sections, even trigger early transition. To approximate the aerodynamic simulation model as close as possible to the real wing with

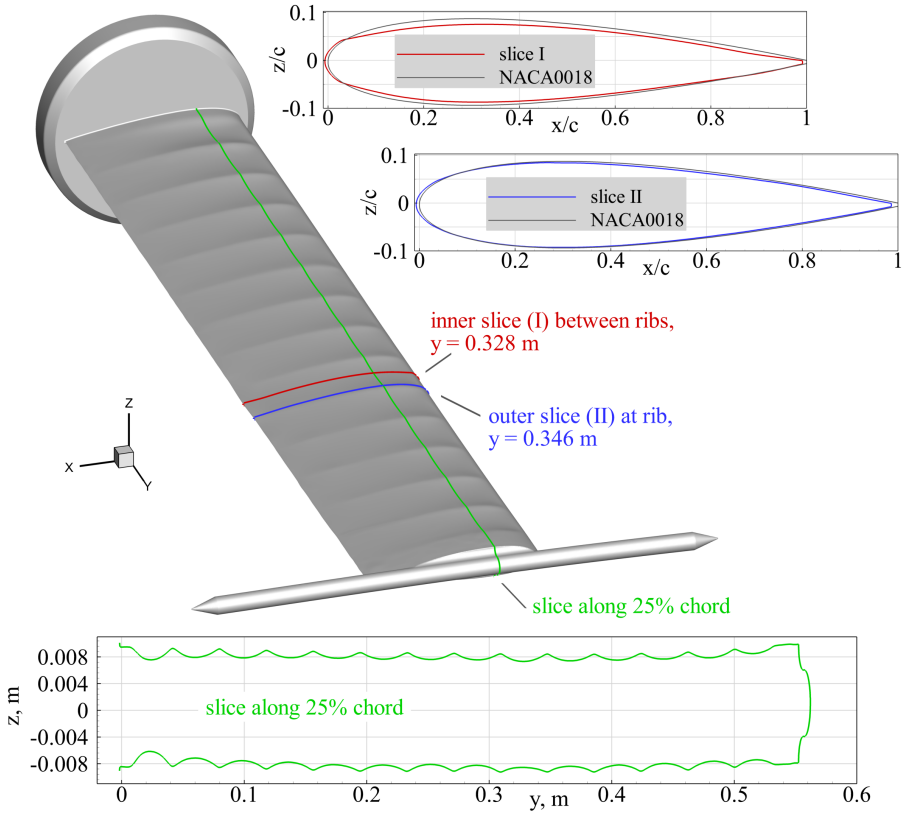

Figure 2: Outer surface of the TU Delft Pazy Wing (from the CFD grid) with cuts at two spanwise sections highlighting the deviations from the theoretical NACA 0018 airfoil section, which is added as reference.

respect to the outer shape, the undeflected jig-shape of the Pazy Wing (without aerodynamic

loading) from TU Delft was digitized using a 3D scanner. Both the cylindrical clamping section as well as the tip rod are included in the scanned surface data. The raw data of the scan were carefully processed and a highly accurate geometry model was generated by NASA which was used for the subsequent CFD grid generation.
The hybrid CFD grid was built with focus on high spatial resolution of the fluid volume close to the wing in order to represent (small) geometrical details and to properly resolve the flow in the boundary layer including laminar separation bubbles as well as regions of separated flow. The surface of the wing (without the tip rod and the cylindrical clamping section) was discretized by a structured (quadrilateral) mesh with small cell sizes both in spanwise and chordwise direction to resolve the complex geometry and the associated flow features. A view of the CFD grid is given in Figure 3.

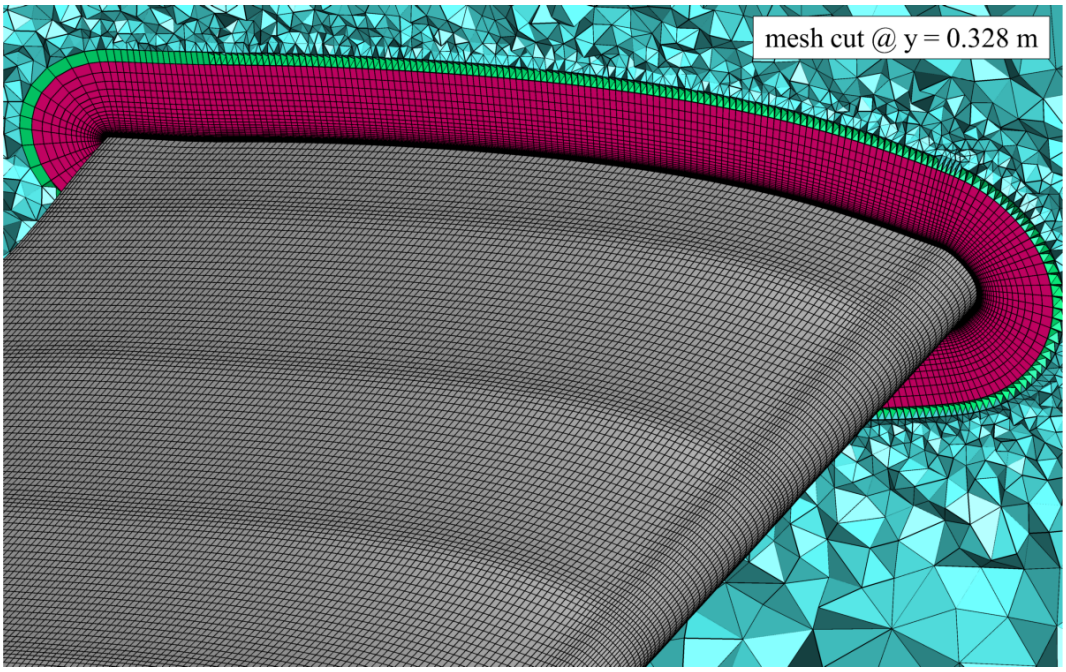

Figure 3: Cut view of the hybrid, unstructured Pazy Wing CFD grid with boundary layer cells. The surface is meshed by structured quadrilaterals.

In addition to the sagged wing, a CFD grid with a similar discretization was built for the clean wing configuration, i.e., without sagging of the foil covering. The geometry model was also built by NASA and as well includes the cylindrical clamping section and the tip rod. The clean configuration is used to analyze the differences to the sagged wing with respect to the flow field and transition mechanisms. Selected parameters of the grid are listed in Table 2.

3 METHODS

3.1 Numerical Setup: DLR computations

The DLR TAU-Code [6] is used in this investigation. The γ transition model [8] is used for transition prediction in combination with the SST k-ω turbulence model with the strain rate based definition of the eddy viscosity [7]. The fully turbulent computations are performed with the SST k-ω turbulence model. For all computations, a central scheme with artificial matrix dissipation is used for the convective flux discretization of the mean flow equations. The convective fluxes of the turbulence equations are discretized with a second-order Roe upwind scheme. A local time step is used in combination with an implicit Backward-Euler scheme to

Table 2: Parameters of the unstructured hybrid CFD grid of the Pazy Wing.

Property	Unit	Pazy Wing CFD grid
Spacing of structured quads chordwise	mm	0.3 - 0.7
Spacing of structured quads spanwise (average)	mm	1.0
first layer thickness	mm	0.0024
Number of layers	-	44
Stretching ratio	-	1.16
Total layer height	mm	10.3
Total number of elements	-	$\approx$ 12000000
Total number of nodes	-	$\approx$ 7200000

accelerate convergence employing an LU-SGS scheme for the steady computations. The dual time stepping scheme by Jameson [10] is used for the unsteady computations.

3.2 Wind Tunnel Experiment: Infrared Thermography Measurements

A wind tunnel experiment is conducted to support the CFD simulation results with validation data for the complex behavior of the boundary layer on the Pazy wing. The experiment is performed at the Open Jet Facility at Delft University of Technology, which has a freestream turbulence intensity of around $Tu = 0.5\,\%$. The test object is the TU Delft Pazy Wing that was previously scanned with the 3D scanner to provide the reference shape for the CFD simulations as mentioned above. For the experiment, the wing is mounted vertically in the wind tunnel test section and subjected to an inflow velocity of $U_\infty = 18\,\mathrm{m/s}$, corresponding to a Reynolds number of approximately $Re_c = 120\,000$, at various angles of attack α in the range $0° < \alpha < 16°$. The measurements are performed with a FLIR SC7300 infrared camera, which is acquiring thermographic images with a resolution of 320 x 256 pixels at a frame rate of $230\,\mathrm{Hz}$. When heating the wing surface above the temperature of the freestream with an external heat source, such as a halogen lamp, the infrared thermography measurements of the wing surface can be used to infer the boundary layer state through the proportionality of skin friction and convective heat transfer [11]. The infrared camera measures the infrared radiation emitted from the surface of the wing, which is proportional to its surface temperature. For this study, the values of the surface temperature are of no direct interest, hence no temperature calibration is performed and the infrared thermographic data is analyzed in terms of the infrared radiation in camera counts. The experimental setup and its components in the wind tunnel are shown in Fig. 4.

4 RESULTS

4.1 Transition Behavior on a NACA0018 Airfoil at Low Reynolds Numbers

This section presents a transition model validation for a NACA0018 airfoil at low Reynolds numbers. The NACA0018 is the theoretical cross section of the Pazy Wing. The γ transition model is built to predict Tollmien-Schlichting transition in transonic high Reynolds number flow [8]. Although there is no lower bound for the model application in terms of Reynolds or Mach number, the γ transition model has not been tested extensively for Reynolds numbers below $Re_c < 10^6$. Especially for heavily separated flows, the prediction of laminar separation bubbles in location, size, and the related transition behavior might be insufficient. The original γ-Re_θ transition model allows an increase of the intermittency up to an effective value of $\gamma_{eff} = 2$ in separated laminar flow to limit the separation bubble size [12]. This model feature is

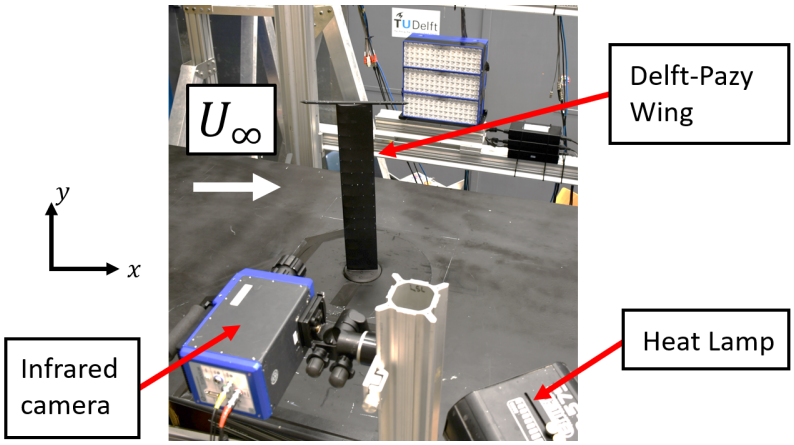

Figure 4: Wind tunnel setup for the infrared thermography measurements.

dropped in the γ model as no systematic over-prediction of laminar bubble sizes is found at high Reynolds numbers, but an increase in effective intermittency might be necessary at lower Reynolds numbers.

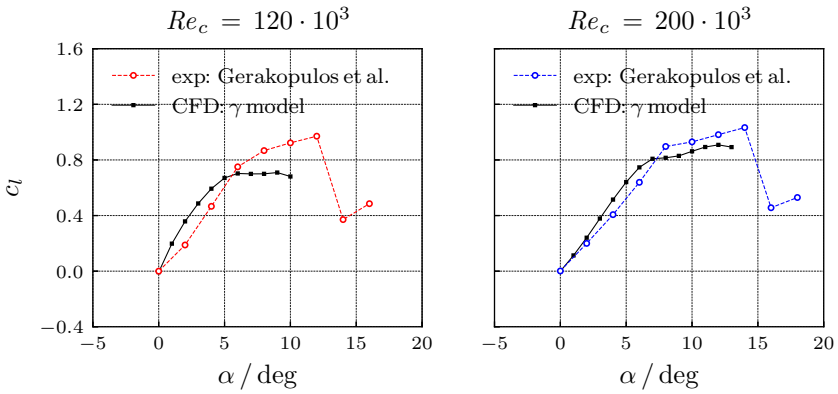

Figure 5: Experimental and computational lift coefficient in subsonic flow of a NACA0018 with free boundary layer transition.

To gain more information on the transition model behavior in low Reynolds number flows, the experimental data by Gerakopulos et al. [13] are used to further validate the γ transition model. Gerakopulos et al. [13] present wind tunnel data for a NACA0018 airfoil at Reynolds numbers ranging from $Re_c = 80 \cdot 10^3$ to $200 \cdot 10^3$ and angles of attack of $\alpha = 0°$ to $18°$. No specific thermodynamic conditions for the experimental setup are given, but as the wind tunnel is of an open-return suction-type, sea level conditions can be expected. According to Gerakopulos et al. [13], the turbulence level in the wind tunnel is below $Tu < 0.3\,\%$.

Computations with the γ transition model for a blunt-edged airfoil of $c = 1\,\mathrm{m}$ chord length are performed at $Re_c = 120 \cdot 10^3$ and $200 \cdot 10^3$ for a subsonic inflow Mach number of $M_\infty = 0.15$ at $T_\infty = 293.15\,\mathrm{K}$ and $Tu = 0.3\,\%$. The computational grid consists of $400\,880$ grid points. The airfoil surface is discretized with a spacing of $\Delta x_s/c \approx 0.002$. The y^+ value of the first cell is well below 1 with maximum values of about $y^+_{max} \approx 0.65$ for the larger angles of attack at $Re_c = 200 \cdot 10^3$. The boundary layer is well covered with a structured mesh consisting of 114 layers with a wall normal growth rate of 1.1 up to a maximum wall normal spacing of $\Delta y_s/c \approx 0.002$. The remaining flow field is discretized using a quad-dominant unstructured grid.

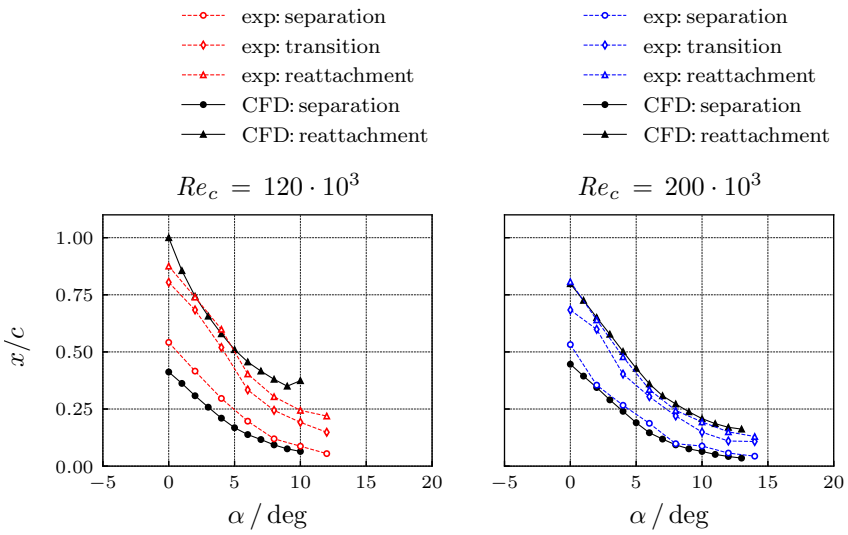

Figure 6: Experimental and computational separation behavior at different Reynolds numbers on the suction side of a NACA0018.

Figure 5 shows the experimental and computational lift coefficient for both Reynolds numbers. Only well converged CFD results are presented, which limits the examination to angles of attack below the lift breakdown. Especially for the lower Reynolds number of $Re_c = 120 \cdot 10^3$, the experiment and CFD computation agree poorly. Neither the lift coefficient, nor the lift curve slope, nor the maximum lift is predicted correctly. The agreement increases strongly with increasing Reynolds number for $Re_c = 200 \cdot 10^3$.

Figure 6 presents the separation behavior on the suction side of the airfoil for increasing angles of attack. The experimental separation behavior is evaluated based on the pressure coefficient distribution, for which a separation point, a transition location, and a reattachment point are identified [13]. The separation and reattachment point in the computation are directly taken as the zero crossing of the skin friction coefficient. Turbulent trailing edge separations are not included, but exist for higher angles of attack. Again, the agreement for the lower Reynolds number of $Re_c = 120 \cdot 10^3$ is poor. The separation location is in much worse agreement than the reattachment location which indicates that the pressure gradient upstream of the separation is not computed correctly. A mismatch in the pressure distribution is most likely caused by a poor agreement in the trailing edge flow, which is determined by the upstream growth of the boundary layer and the predicted separation and transition behavior. In contrast, the results for $Re_c = 200 \cdot 10^3$ agree very well with the experimental data.

The transition location for the γ transition model is not easily defined which is especially true for separated flow. It is therefore not compared to the experimental data presented by Gerakopulos et al. [13]. The intermittency variable γ of the transition model is a blending function for the turbulence model. Once the transition criterion is fulfilled, the intermittency increases and production of turbulence kinetic energy starts. The transition criterion is based on experimental data but the actual model onset does not represent a meaningful location within the transition process like the indifference Reynolds number, at which disturbances start to grow, or the critical Reynolds number, at which the transition process is completed. The intermittency in the model has to increase and spread within the boundary layer to allow for any change in the boundary layer. The offset between model onset and the fully developed turbulent boundary

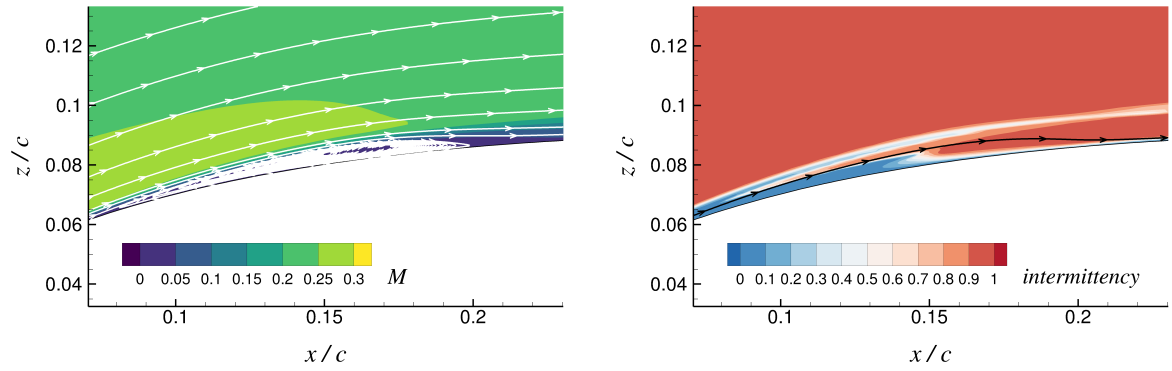

Figure 7: Mach number and intermittency field at the separation bubble location on the suction side of a NACA0018 at $\alpha = 10°$, $Re_c = 200 \cdot 10^3$, $M = 0.15$ with velocity streamlines.

layer state is part of the transition model calibration. The transition process itself has to be identified by secondary parameters like the skin friction coefficient distribution.

Figure 7 shows the Mach number and intermittency field at the separation bubble location on the suction side of the NACA0018 at $\alpha = 10°$, $Re_c = 200 \cdot 10^3$, $M = 0.15$. The streamlines in the left part of the Figure show the recirculation area within the separation bubble (separation at $x/c \approx 0.064$, reattachment at $x/c \approx 0.208$). The first intermittency increase is found at $x/c \approx 0.08$ but only the strong increase of intermittency in the recirculation area enables the reattachment due to the subsequent increase in turbulence kinetic energy. A transition location might be defined based on a certain threshold of a turbulence model variable (e.g. $R_t = \mu_t/\mu > 1$) but this choice might be quite arbitrary.

4.2 Steady CFD Results for the Clean and Sagged Pazy Wing

This section presents steady results for the clean and sagged Pazy Wing. The steady computations are performed at $U_\infty = 50\ \mathrm{m/s}$ at sea level conditions with $\rho_\infty = 1.225\ \mathrm{kg/m^3}$, $T_\infty = 288.15\ \mathrm{K}$, $p_\infty = 101\,325\ \mathrm{Pa}$, resulting in a Reynolds number of $Re_c = 342\,165$ for $c = 0.1\,\mathrm{m}$ and a Mach number of $M = 0.1469$. Although the experimental data presented in Sec. 4.4 is given at a lower flow speed of $U_\infty = 18\ \mathrm{m/s}$ and subsequently at a lower Reynolds number of $Re_c = 120\,000$, the comparison with the experimental data of Gerakopulos et al. [13] indicates that such low Reynolds numbers are not predicted reliably. As indicated below, the comparison of the CFD and experimental data still provides a valuable insight into the actual flow phenomena occurring on the Pazy Wing and into the predictive capabilities of local intermittency transport transition models. A turbulence level of $Tu = 0.3\,\%$ is kept in the computations to have a consistent numerical setup with the data presented in the previous section.

Figures 8 and 9 show the fully turbulent and transitional aerodynamic coefficients for the clean and sagged Pazy Wing configuration, respectively. Figure 10 compares the transitional results for both configurations obtained with the γ transition model. Neither the transitional computations with the γ transition model, nor the fully turbulent computations with the SST k-ω model converge to a steady result but oscillate about some mean value. This unsteady flow behavior is caused by boundary layer separations. Therefore, Figs. 8 to 10 give the mean value and the magnitude of the oscillation indicated by error bars. The transitional results do not necessarily show a worse convergence behavior compared to the fully turbulent computations.

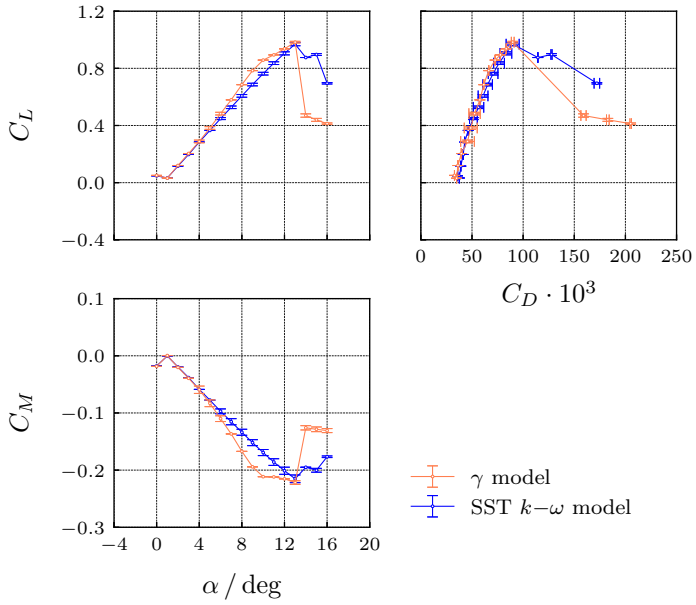

Figure 8: Transitional and fully turbulent aerodynamic coefficients for the clean Pazy Wing configuration.

For the clean wing configuration, the lift and moment increase for the transitional flow is only slightly larger than for the fully turbulent flow for low angles of attack. For larger angles of attack, a stronger deviation between the fully turbulent and transitional results is obtained. A similar behavior is observed for the sagged wing configuration. In addition, a laminar drag bucket is found for the sagged wing around $\alpha = 0°$ with the characteristic increase in lift and moment. A laminar drag bucket usually occurs due to a decrease in the displacement thickness on the upper surface and a drag decrease due to a large amount of laminar boundary layer flow. For a case of spanwise varying heavily separated flow in combination with boundary layer transition, the effect is more obscure and will need further investigations.

Figures 11 and 12 show the skin friction coefficient distribution for increasing angles of attack on the upper surface of the clean and sagged wing configuration, respectively. The black line gives the zero crossing of the skin friction value indicating separated flow regions. For the clean wing configuration in Fig. 11, a laminar separation bubble develops on the upper surface similar to the experimental and CFD results shown in Sec. 4.1 for the NACA0018 airfoil. As the angle of attack increases, the separation bubble moves upstream due to the stronger adverse pressure gradient and reduces in size. The laminar separation bubble covers the whole wing span with the exception of the wing tip area where the chordwise flow is influenced by the wing tip vortex. At about $\alpha = 10°$, a turbulent trailing edge separation starts to develop which causes a reduced lift and moment curve slope as seen in Fig. 8. As the angle of attack is increased further, the flow on the upper wing surface is completely separated and the lift breakdown occurs.

The boundary layer flow on the sagged wing configuration is much more complex compared to the clean wing. At each rib location the originally intended shape of the wing is obtained. In between the rib locations, the shape is lost and the local profile is thinner and has a kink in spanwise direction. At the kink location, pockets of separated flow occur. For $\alpha = 0°$, the boundary layer flow downstream of the separation bubble is still laminar as a spanwise flow from the ribs into the sagged regions occurs, that might stabilize the laminar flow. The intermittency only increases directly at the bubble location but vanishes further downstream. A further

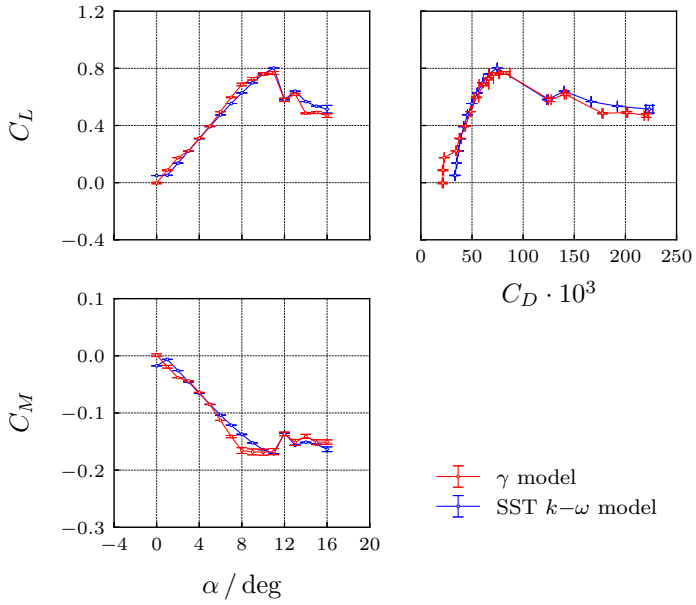

Figure 9: Transitional and fully turbulent aerodynamic coefficients for the sagged Pazy Wing configuration.

discussion requires more unsteady CFD computations, which are not available at the moment. Further downstream, laminar separation bubbles develop over the whole wing span. The laminar boundary layer separates further downstream at the rib locations compared to the sagged areas. As the angle of attack is increased, the boundary layer reattaches in a fully turbulent state downstream of the leading edge separations (seen by high skin friction values downstream of the separation bubble). Once the boundary layer flow becomes turbulent, the boundary layer can withstand the drag increase towards the trailing edge and a more complicated pattern of separated and attached boundary layer flow develops. As the angle of attack is increased, the leading edge separations at the kink grow in stream and spanwise size with a subsequent increase of regions with turbulent boundary layer flow downstream. At the same time, the laminar separations at the rib locations move upstream and decrease in size. As the maximum lift is approached, turbulent trailing edge separations develop in the sagged regions. A further increase in angle of attack results in a completely separated flow on the upper surface.

Figure 13 shows skin friction lines for some angles of attack on the upper surface of the sagged wing. In between the leading edge separation bubbles, the entrainment effect is visible as the skin friction lines bend towards the sagged regions of the wing. For $\alpha = 6°$, a sagged and a rib location are labeled in Fig. 13 with *Pos. I* and *Pos. II*, respectively. The geometry, pressure coefficient and skin friction distribution are shown in Fig. 14. The kink that occurs for the sagged area at *Pos. I* causes a strong pressure increase which causes the laminar boundary layer to separate, undergo transition along the separation bubble and to reattach in a fully turbulent state as can be seen in the strong increase in skin friction downstream of the separation bubble. Simultaneously, the suction peak at the rib location is not strong enough to cause transition and a laminar separation bubble develops further downstream.

4.3 Unsteady CFD Results for the Clean and Sagged Pazy Wing

Unsteady computations are performed to evaluate how much the time resolved flow differs from the steady solution. A time step size of $\Delta t = 2 \cdot 10^{-4}\,\mathrm{sec}$ is used, which is small enough to resolve the most important flow features. The number of inner iterations is chosen to give well

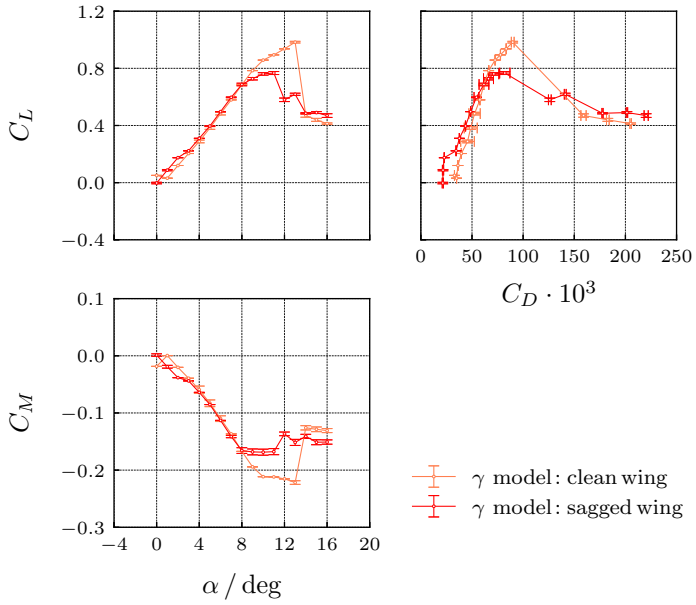

Figure 10: Transitional aerodynamic coefficients for the clean and sagged Pazy Wing configuration.

converged results within each time step for the dual time stepping scheme. Figure 15 shows the time series and amplitude spectrum of the unsteady lift coefficient for the clean and sagged wing at $\alpha = 6°$. The full and dashed red lines represent the mean value and the magnitude of the oscillations in the steady computations, respectively. The amplitude spectrum is computed for the last $0.15\,\mathrm{sec}$ only to exclude any transient behavior in the spectrum. The unsteady oscillations of the lift coefficient are similar for both configurations in terms of magnitude and frequency as can be seen from the amplitude spectrum of the lift coefficient. In contrast, the steady computations for the clean wing show much larger deviations from the mean compared to the steady computations for the sagged wing. A first evaluation of the unsteady data indicates that the unsteadiness of the flow is linked to the circular wind tunnel model support, but further investigations are required at this point.

4.4 Experimental Validation

The numerical results for the skin friction distribution on the suction side of the wing are validated against the experimental measurements with the infrared camera in the wind tunnel. A direct quantitative comparison is not performed due to the differences in Reynolds number between the experiment ($Re_c = 120\,000$) and the simulation ($Re_c = 340\,000$). However, it is expected that a qualitative comparison is still suitable as a validation of the numerical results because the qualitative behavior of the boundary layer does not change drastically in the considered range of Reynolds numbers, based on the results from Gerakopulos et al. [13] shown in Fig. 6. The infrared images for increasing angles of attack from $\alpha = 0°$ to $\alpha = 16°$ are shown in Fig. 16.

The images in Fig. 16 show a section of around $250\,\mathrm{mm}$ of the wingspan, which is located at approximately mid-span. The displayed images are the temporal averages from a time series of 1000 acquired images for each α, to diminish the effect of random measurement errors. Apart from this, no further processing is applied to the infrared image data.

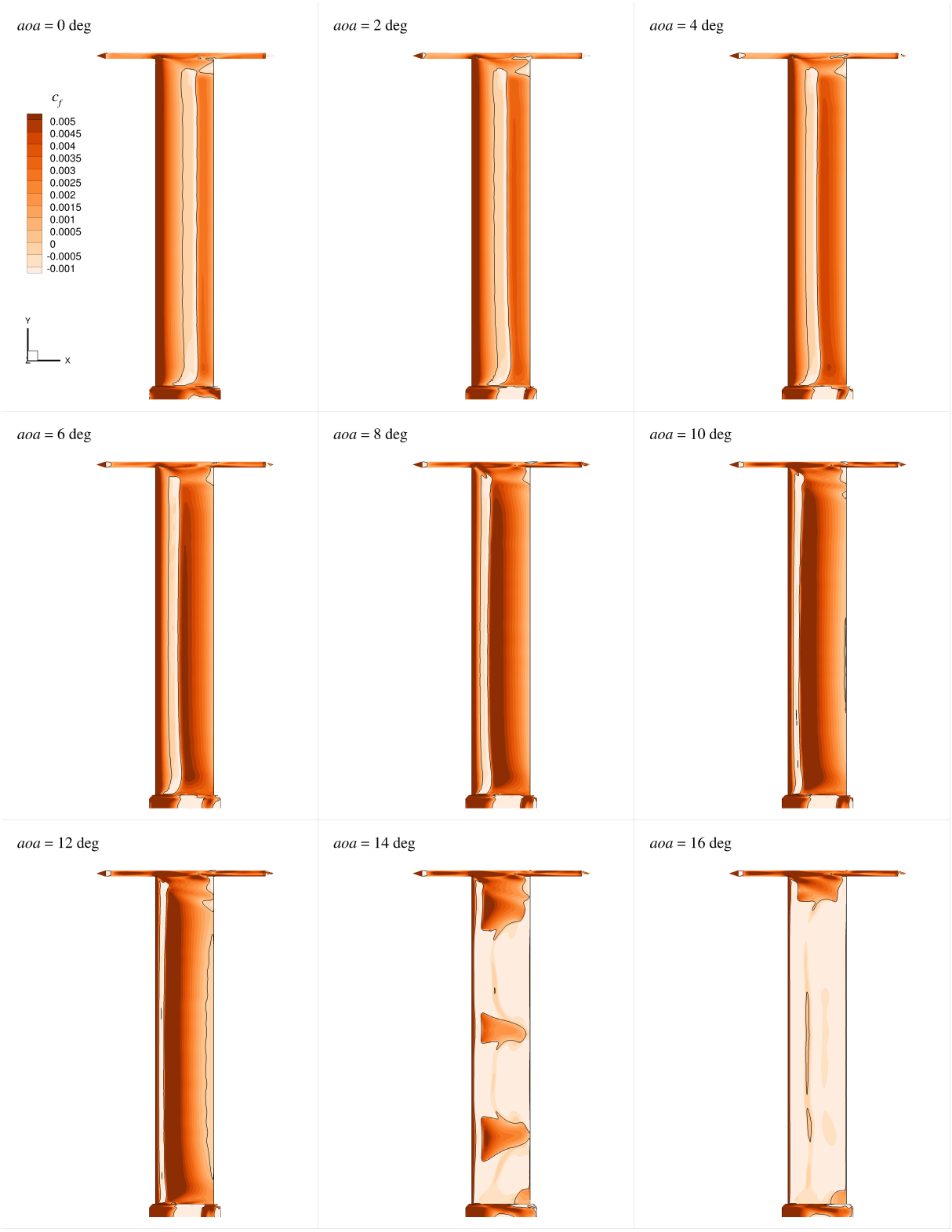

Figure 11: Skin friction coefficient distribution on the clean wing for increasing angles of attack for the transitional flow. The black line gives the zero crossing of the skin friction value.

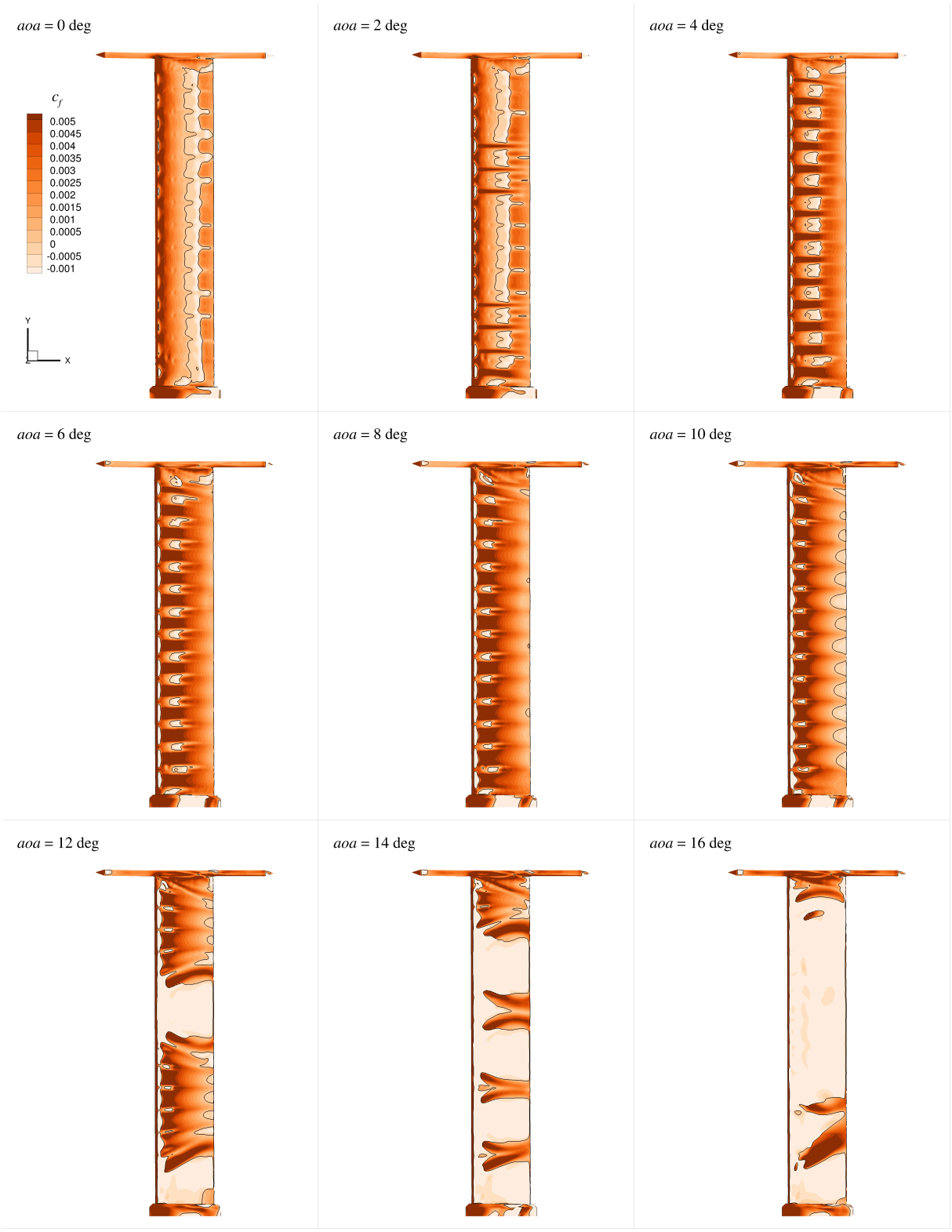

Figure 12: Skin friction coefficient distribution on the sagged wing for increasing angles of attack for the transitional flow. The black line gives the zero crossing of the skin friction value.

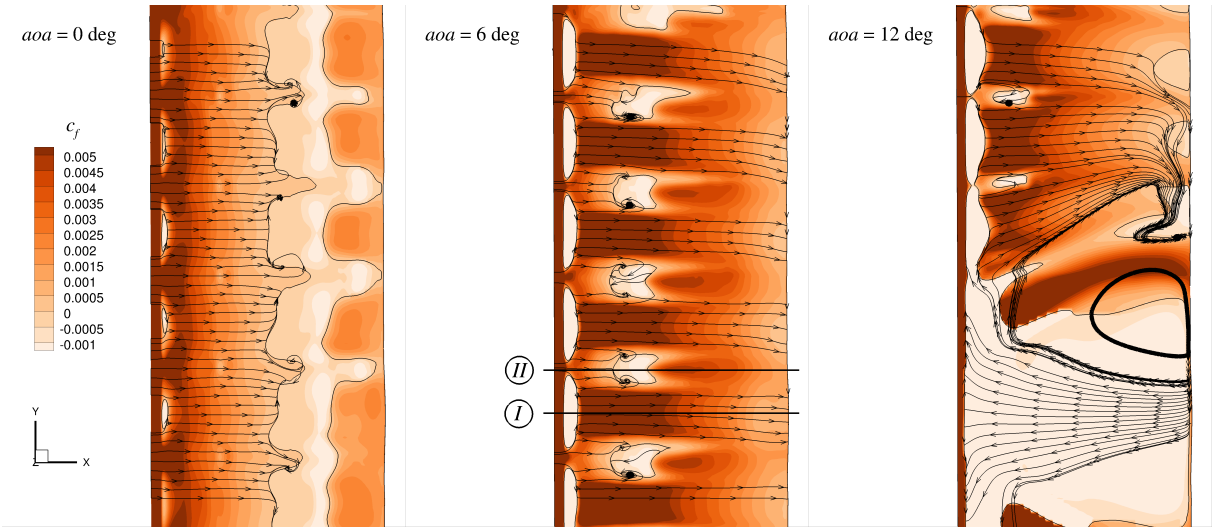

Figure 13: Skin friction coefficient distribution and skin friction lines on the sagged wing for increasing angles of attack in the range $y = 0.28\,\mathrm{m}$ to $0.5\,\mathrm{m}$ for the transitional flow. The black line gives the zero crossing of the skin friction value.

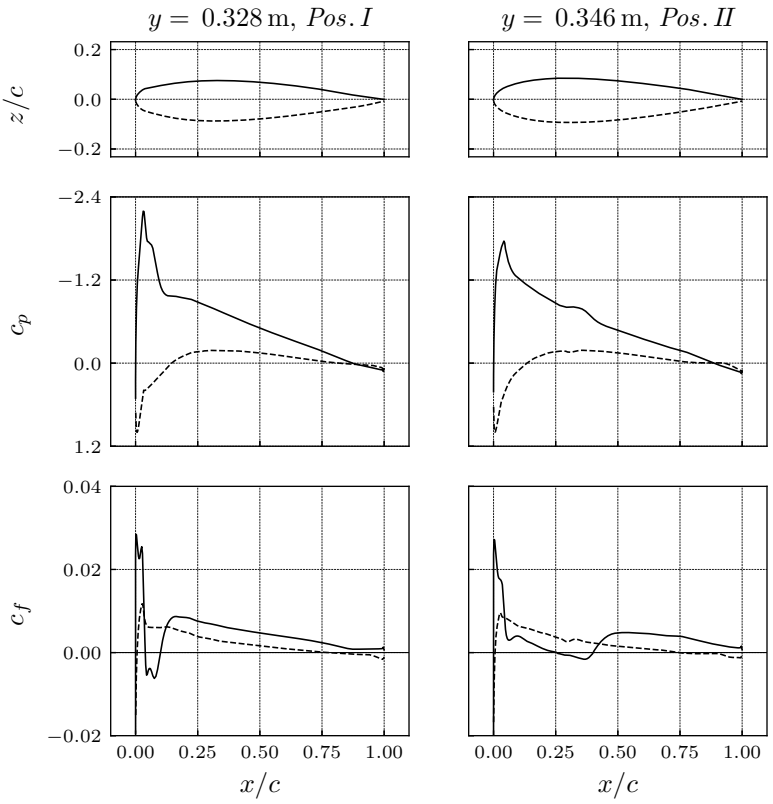

Figure 14: Geometry, pressure coefficient, and skin friction coefficient distribution at a sagged (*Pos. I*) and rib location (*Pos. II*) at $\alpha = 6°$ for the transitional flow.

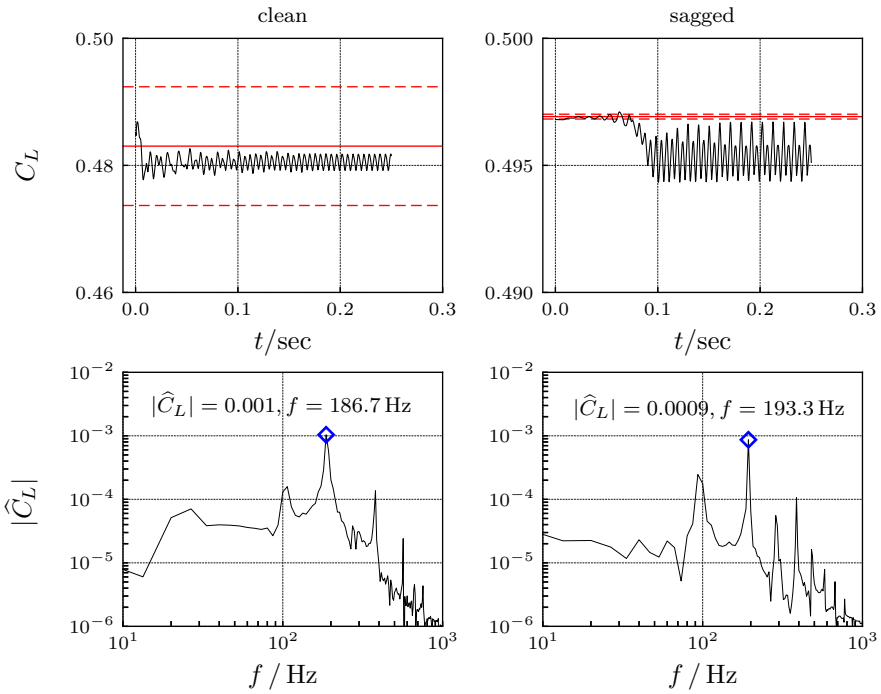

Figure 15: Time series and amplitude spectrum of the unsteady lift coefficient for the clean and sagged wing at $\alpha = 6°$. The full and dashed red lines give the mean value and the magnitude of the oscillations in the steady computations, respectively.

The infrared thermography measurements shown in Fig. 16 are in very good agreement with the skin friction results shown in Fig. 12 over the entire range of the considered angles of attack. For $\alpha = 0°$, a region of increased surface temperature is present, at approximately $x/c = 0.55$ to $x/c = 0.75$ and relatively uniform along the span, which can be linked to the region of separated flow and thus reduced convective heat transfer at this angle of attack that was observed in the CFD simulations. As the angle of attack increases, the spanwise differences of the TU Delft Pazy Wing, in terms of the cross-sectional shape on the rib locations and between them, cause significant differences in the spanwise flow pattern. The main effect that is visible in the experimental data is a reduced surface temperature downstream of the kink near the leading edge in the airfoil shape between the rib locations, suggesting that this kink causes the boundary layer to transition to turbulence and thus increasing the skin friction and with that the convective heat transfer when compared to a laminar boundary layer state. As it was observed in the CFD simulations, this effect sets in locally at individual spanwise locations at $\alpha = 2°$, and is fully established at $\alpha = 4°$. When further increasing α, the region of turbulent flow covers a larger fraction of the span in the simulation and in the experiment, as observed in 16 through the increasing width of the darker region of lower surface temperature. For very high values of α, the flow over the wing appears as fully turbulent at $\alpha = 12°$, before at $\alpha = 14°$, local flow separation effects cause an increased surface temperature at some sections of the span, before full stall is reached at $\alpha = 16°$, indicated by a generally increased surface temperature in comparison to the turbulent attached flow. These experimental observations for very high angles of attack are in very good qualitative agreement with the CFD results shown in Fig. 12 as well.

A more detailed discussion of the experimental results and in particular of the laminar separation bubble that forms with increasing α behind the kink in the airfoil shape between the ribs can be

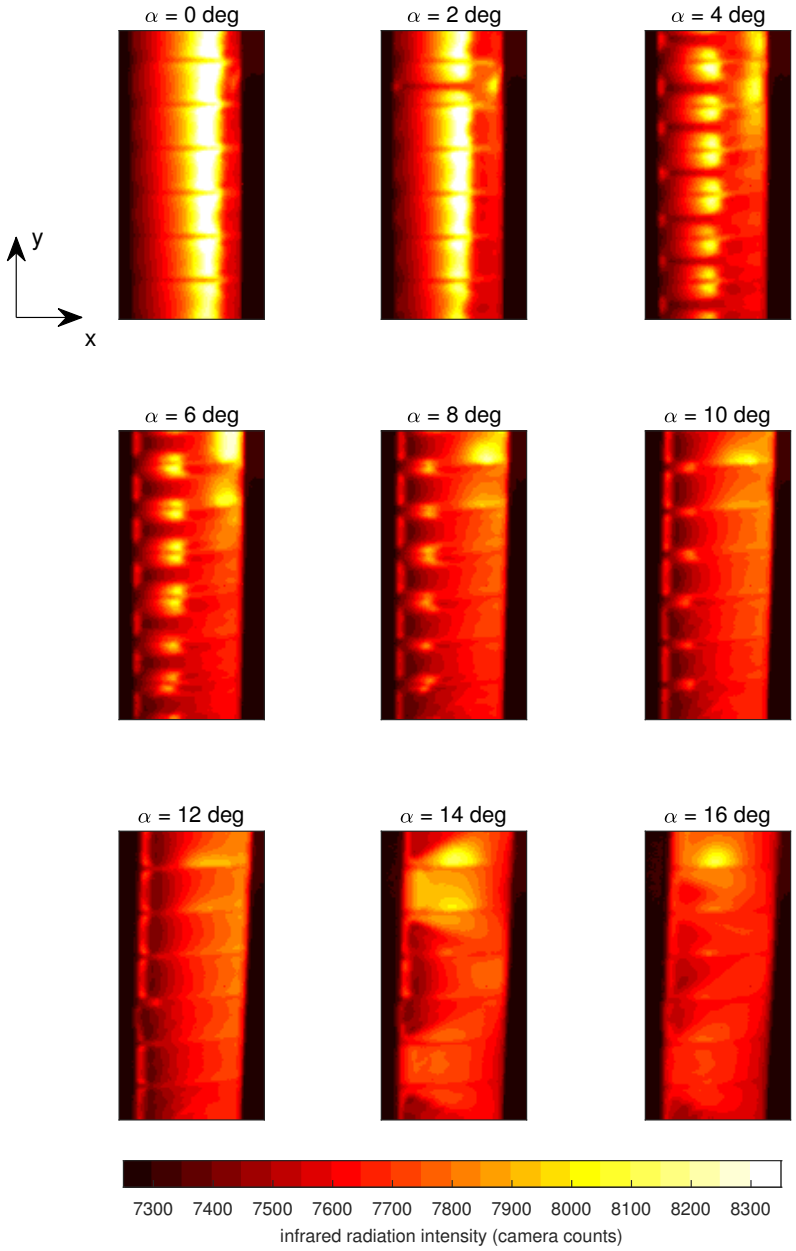

Figure 16: Infrared thermography images at various angles of attack.

performed by inspecting the experimental temperature profiles at two different locations Pos. I and Pos. II, in between and directly on the ribs respectively, as it was done for the simulation results shown in Fig. 14. For the experimental data, this is done by first detecting the leading and trailing edge of the wing in the infrared images and then mapping the measurements on the chordwise location. The results for the temperature distributions in terms of the infrared radiation intensity for three different angles of attack at the two considered spanwise positions are shown in Fig. 17.

As visible in Fig. 17, the chordwise temperature distributions are similar between Pos. I and Pos. II for $\alpha = 2°$, and strongly deviate between the two positions for the larger angles of attack. At $\alpha = 2°$, the temperature increases in the chordwise direction, first slightly, which is related to the chordwise decrease in skin friction and heat transfer associated with the growth in laminar boundary layer thickness, and then more steeply as the flow separates and forms a laminar separation bubble. At around $x/c = 0.7$, the flow transitions to turbulence and

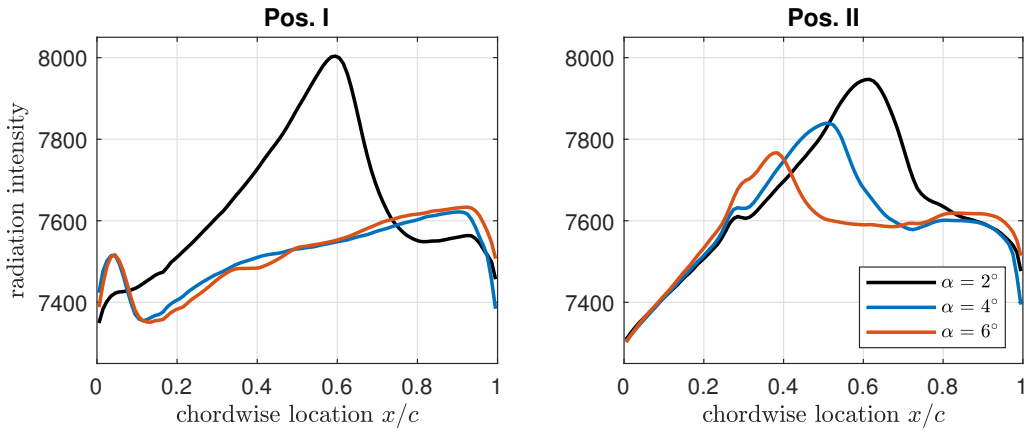

Figure 17: Chordwise temperature distributions between two ribs (Pos. I) and on a rib (Pos. II).

subsequently reattaches, causing a steep temperature drop. A qualitatively identical behavior is observed at Pos. II for the higher angles of attack as well, where the location of the laminar separation bubble and the transition location are moving consistently upstream with increasing α. Different behavior is observed at Pos. I, where a steep rise in the temperature is formed directly downstream of the leading edge as the angle of attack is increased above $\alpha = 2°$. This can be linked to the region of separated flow that was observed in the CFD simulations to form downstream of the kink in the airfoil shape near the leading edge. Downstream of the bubble location, after around $x/c = 0.1$ for $\alpha = 4°$ and $\alpha = 6°$, the surface temperature is lower than at $\alpha = 2°$, which can be explained by the higher convective heat transfer level that is associated with a turbulent boundary layer. This confirms that the kink in the airfoil in between the ribs is responsible for triggering the transition to turbulence over a laminar separation bubble, as observed in the CFD simulation results.

5 CONCLUSIONS

This paper presents CFD results in support of the 3rd *Aeroelastic Prediction Workshop*. The CFD data is contrasted with experimental data to validate the predicted transition behavior qualitatively. In the computations, the γ transition model is used. This model is built and validated for high Reynolds number and high Mach number flows. Therefore, the model's predictive capabilities are first tested on experimental data for a NACA0018 representing the theoretical cross-sectional geometry of the Pazy Wing. The computations at $Re_c = 200 \cdot 10^3$ show a good agreement in the size of a laminar separation bubble, which indicates a well predicted transition behavior. The agreement in the aerodynamic coefficients is lower but might be attributed to wind tunnel effects. For the lower Reynolds number of $Re_c = 120 \cdot 10^3$, the prediction of the laminar separation bubble observed experimentally deteriorates strongly. Based on this observation, the CFD computations for the Pazy Wing are performed at a higher flow speed i.e. higher Reynolds number compared to the TU Delft wind tunnel experiment. Computations for a clean wing configuration with the theoretical wing geometry and for a sagged wing geometry are performed. For the clean wing, the separation behavior is quite similar to the airfoil data. In contrast, the sagged wing shows a very complex boundary layer flow, for which spanwise varying segments of laminar and fully turbulent flow are found. Depending on the upstream boundary layer state, a very different separation behavior is observed. The data from the wind tunnel experiment show the same behavior on a qualitative level. In addition, a laminar separation bubble found at the leading edge within the sagged regions could also be verified through an inspection of the experimental temperature profiles. For most cases, no steady solution is found

in the CFD computations and only preliminary unsteady computations could be performed for a single angle of attack. Therefore, any interpretation of flow phenomena should be done with caution as a complete set of unsteady computations for the whole lift curve would be necessary. However, the agreement between experimental and CFD data is already satisfying albeit the higher Reynolds number in the computations. In addition, the complex flow on the Pazy Wing is fully captured by the local correlation-based transition model approach with a minimum of additional user input compared to a fully turbulent computation.

6 ACKNOWLEDGMENTS

The work of NASA to generate a highly accurate geometry file for the generation of the CFD grid based on the scanned outer surface of the TU Delft Pazy Wing is gratefully acknowledged. As well, the support of the DLR Institute of Aeroelasticity for this work is acknowledged. Furthermore, the help of the members of the LDWG of the AePW3 is appreciated.

7 REFERENCES

[1] Avin, O., Raveh, D. E., Drachinsky, A., and Ben-Shmuel, Y. (2021). An Experimental Benchmark of a Highly Flexible Wing, AIAA SciTech 2021 Forum.

[2] Riso, C. and Cesnik, C. E. S. (2021). Correlations Between UM/NAST Nonlinear Aeroelastic Simulations and the Pre-Pazy Wing Experiment, AIAA Scitech 2021 Forum.

[3] Goizueta, N., Drachinsky A., Wynn, A., Raveh, D. E., and Palacios, R. (2021). Flutter predictions for very flexible wing wind tunnel test, AIAA Scitech 2021 Forum.

[4] Drachinsky, A. and Raveh, D. E. (2021). Nonlinear Aeroelastic Analysis of Very Flexible Wings Using the Modal Rotation Method, AIAA Scitech 2021 Forum.

[5] Hilger, J. and Ritter, M. R. (2021). Nonlinear Aeroelastic Simulations and Stability Analysis of the Pazy Wing Aeroelastic Benchmark, MDPI Aerospace.

[6] Schwamborn, D., Gerhold, T., and Heinrich, R. (2006). The DLR TAU-Code: Recent Applications in Research and Industry. In: Proceedings European Conference on Computational Fluid Dynamics ECCOMAS, Delft.

[7] Menter, F. R., Kuntz, M., and Langtry, R. (2003). Ten Years of Industrial Experience with the SST Turbulence Model. In: Turbulence, Heat and Mass Transfer 4, ed: K. Hanjalic, Y. Nagano, and M. Tummers, Begell House, Inc., 625–632.

[8] Fehrs, M. (2018). Boundary Layer Transition in External Aerodynamics and Dynamic Aeroelastic Stability. Dissertation, TU Braunschweig, ISSN 1434-8454, ISRN DLR-FB-2018-11, also NFL-FB 2017-27, Braunschweig.

[9] Krumbein, A., Krimmelbein, N., and Schrauf, G. (2009). Automatic Transition Prediction in Hybrid Flow Solver, Part 1: Methodology and Sensitivities. *Journal of Aircraft*, 46(4), 1176–1190.

[10] Jameson, A. (1991). Time dependent calculations using multigrid, with applications to unsteady flows past airfoils and wings. 10^{th} Computational Fluid Dynamics Conference, AIAA, 91-1596, Honolulu.

[11] de Luca, L., Carlomagno, G.M., and Buresti, G. (1990). Boundary layer diagnostics by means of an infrared scanning radiometer. *Experiments in Fluids*, 9, 121–128, https://doi.org/10.1007/BF00187411

[12] Langtry, R. B. and Menter, F. R. (2009). Correlation-Based Transition Modeling for Unstructured Parallelized Computational Fluid Dynamics Codes. *AIAA Journal*, Vol. 47, No. 12, 2894–2906.

[13] Gerakopulos, R., Boutilier, M. S. H., and Yarusevych, S. (2010). Aerodynamic Characterization of a NACA 0018 Airfoil at Low Reynolds Numbers. 40^{th} Fluid Dynamics Conference and Exhibit, AIAA, 2010-4629, Chicago.

COPYRIGHT STATEMENT